

## Atmospheric effects in interferometric synthetic aperture radar surface deformation and topographic maps

Howard A. Zebker

Department of Electrical Engineering and Department of Geophysics, Stanford University, Stanford, California

Paul A. Rosen and Scott Hensley

Jet Propulsion Laboratory, California Institute of Technology, Pasadena

**Abstract.** Interferogram images derived from repeat-pass spaceborne synthetic aperture radar systems exhibit artifacts due to the time and space variations of atmospheric water vapor. Other tropospheric variations, such as pressure and temperature, also induce distortions, but the effects are smaller in magnitude and more evenly distributed throughout the interferogram than the wet troposphere term. Spatial and temporal changes of 20% in relative humidity lead to 10 cm errors in deformation products, and perhaps 100 m of error in derived topographic maps for those pass pairs with unfavorable baseline geometries. In wet regions such as Hawaii, these are by far the dominant errors in the Spaceborne Imaging Radar-C and X Band Synthetic Aperture Radar (SIR-C/X-SAR) interferometric products. The unknown time delay from tropospheric distortion is independent of frequency, and thus multiwavelength measurements, such as those commonly used to correct radar altimeter and Global Positioning System (GPS) ionospheric biases, cannot be used to rectify the error. In the topographic case, the errors may be mitigated by choosing interferometric pairs with relatively long baselines, as the error amplitude is inversely proportional to the perpendicular component of the interferometer baseline. For the SIR-C/X-SAR Hawaii data we found that the best (longest) baseline pair produced a map supporting 100 m contouring, whereas the poorest baseline choice yielded an extremely noisy topographic map even at this coarse contour interval. In the case of deformation map errors the result is either independent of baseline parameters or else very nearly so. Here the only solution is averaging of independent interferograms, so in order to create accurate deformation products in wet regions many multiple passes may be required. Rules for designing optimal data acquisition and processing sequences for interferometric analyses in nondesert parts of the world are (1) to use the longest radar wavelengths possible, within ionospheric scintillation and Faraday rotation limits, (2) for topography, maximize interferometer baseline within decorrelation limits, and (3) for surface deformation, use multiple observations and average the derived products. Following the above recipe yields accuracies of 10 m for digital elevation models and 1 cm for deformation maps even in very wet regions, such as Hawaii.

### Introduction

Interferometric radar remote sensing techniques are those in which the phase difference “image,” or interferogram, of radar image pairs is the prime observable, with geophysical descriptions of the surface derived thence. Here we report phase distortions in radar interferograms due most likely to variations in atmospheric water vapor. Since the effect is evidenced as a nearly constant time delay of the radar signal, independent of frequency at microwave wavelengths, the contamination of the signal cannot be mitigated by dual-frequency measurements such as those commonly utilized for ionospheric corrections.

Radar interferometry from space has been applied increasingly often in the last decade for the measurement of the Earth’s topography (see, for example, Zebker *et al.* [1994a, c] for technique description and review), surface velocities (as in

the case of ice flow analysis [Goldstein *et al.*, 1993; Kwok and Fahnestock, 1996; Rignot *et al.*, 1995], and for surface deformation studies [Massonnet *et al.*, 1993, 1994; Zebker *et al.*, 1994b; Peltzer *et al.*, 1994; Peltzer and Rosen, 1995]. Each of these techniques follows from analysis of the phase of radar interferograms, formed by coherent conjugate superposition of complex radar images of a scene acquired from nearly the same viewing angle but at different times.

In the case of topographic analysis, knowledge of the viewing geometry and precise spatial relationship of the two imaging orbits, the interferometer “baseline,” permits reconstruction of the surface topography from the two-dimensional phase field measurements. For the velocity and deformation studies the topographic phase term is minimized or removed by combining three radar images, by independent knowledge of the topography, or by fortunate orbital geometry resulting in a very small spatial baseline. The remaining phase residual is then interpreted as a change in distance with time, or radar “range,” from each point in the scene to the radar platform.

Clearly, any interferometric technique will be compromised

Copyright 1997 by the American Geophysical Union.

Paper number 96JB03804.  
0148-0227/97/96JB-03804\$09.00

if propagation effects such as spatially variable time delays in the propagation medium alter the observed phase significantly. Here we will quantify delays observed in several radar interferograms acquired by the Spaceborne Radar Laboratory (SRL), composed of the Spaceborne Imaging Radar-C and X band Synthetic Aperture Radar SIR-C/X-SAR radar instrumentation. We choose this data set because of the availability of multiwavelength observations, globally distributed coverage, and signals which are characterized by high signal to noise ratio, minimizing other processing artifacts.

Phase defects of unknown, but possibly atmospheric, origin in interferometric SAR have been noted on several previous occasions. That they were due to variability in the atmosphere was a speculation offered by *Massonnet et al.* [1995] and *Massonnet and Feigl* [1995] to explain unknown features in interferograms of Mount Etna and Landers, California. *Rosen et al.* [1996] provide an initial look at the possible mechanisms for atmospheric signatures in SIR-C data acquired over the island of Hawaii. The first analysis of phase defects in SIR-C radar interferograms has recently been reported by *Goldstein* [1995], who found that interferograms acquired over the Mojave Desert in California by SIR-C contained one-way travel errors, expressed as distance, of 0.3 cm rms spread throughout the radar image, with a peak value of 2.8 cm. As will be discussed below, this corresponds to an rms phase noise of 0.16 rad at the L band wavelength and 0.63 rad at the C band wavelength in the radar interferograms. These errors were spatially unrelated to surface features and exhibited the characteristic Kolmogorov 8/3 power law spectrum associated with turbulence.

It is our purpose here to examine in detail similar phase defect data acquired by the SIR-C sensor over the island of Hawaii, to understand their relation to physical characteristics of the troposphere, and to assess their impact on the performance of spaceborne interferometric radar topographic and surface deformation measurement systems. The structure of this paper is as follows. First, we will develop a model of atmospheric effects in repeat-pass radar interferograms and estimate the interferogram degradation expected from typical atmospheric conditions. We next evaluate the severity of the effect as it applies to several common geophysical applications and find that for the topography case the error from the atmospheric irregularities is highly dependent on baseline length, while for deformation studies, baseline is unimportant, and that in both cases the distortions provide an effective "noise floor" for observations that varies with the change in humidity of the scene locale. We will analyze data acquired over a very wet region (Hawaii), which makes the effects that much more obvious, and compare the magnitude of the fluctuations with those reported over the California desert by *Goldstein* [1995]. Finally, we discuss methods to reduce or eliminate these distortions in practical systems.

### Effect of Atmospheric Variability on Radar Propagation

Interferometric radar analyses follow from interpreting the precise time delays and differential phase shifts in radar echoes as distance measurements and relating those geometric distances to topography, motion, or deformation of the surface. The geometric relations are illustrated in Figures 1a and 1b, which define the topographic and motion measurements in terms of viewing geometry and radar-measurable distances (see, for example, *Zebker et al.* [1994b] for a derivation). We

generally assume that the signals propagate at known constant velocity to convert the time delays and phase shifts to distance. However, if the signals propagate through the spatially inhomogeneous Earth's atmosphere, which has a slightly higher index of refraction than free space, the velocity is lowered slightly, leading to spatially variable delays which contaminate the observations.

Denote the complex amplitude of a unit intensity plane wave at position  $x$  in a medium with variable refractive index  $n(x)$  and wavelength  $\lambda$  by

$$\mathbf{E} = e^{j(kx - \omega t)} \quad (1)$$

where the wavenumber  $k = 2\pi n(x)/\lambda$ . Differentiating yields the following relation between incremental path length  $dx$  and incremental signal phase  $d\phi$ :

$$d\phi = \frac{2\pi n(x)}{\lambda} dx \quad (2)$$

Integrating along the propagation path, we obtain

$$\phi = \int_x \frac{2\pi n(x)}{\lambda} dx \quad (3)$$

For a radio signal propagating through free space,  $n(x) = 1$ , and the phase shift is directly proportional to path length:

$$\phi = \frac{2\pi}{\lambda} x \quad (4)$$

Here the phase shift  $\phi$  depends only on the free-space wavelength  $\lambda$  and the distance propagated  $x$ . If the signal propagates instead through an atmosphere,  $n(x)$  is not constant and an additional phase shift follows. For the Earth's neutral atmosphere,  $n(x)$  is always real and slightly greater than one, so we can expand  $n(x)$  as  $1 + 10^{-6}N(x)$ , where  $N(x)$ , called the refractivity, is the additional refractive index due to the atmosphere. The change in  $n(x)$  from the free space value of 1 is very small for Earth's atmosphere, leading to the factor of  $10^{-6}$  in the definition. In this case, equation (4) becomes

$$\phi = \frac{2\pi}{\lambda} x + \frac{2\pi 10^{-6}N(x)}{\lambda} x \quad (5)$$

or

$$\phi = \frac{2\pi}{\lambda} x + \frac{2\pi}{\lambda} \Delta x \quad (6)$$

where  $\Delta x = 10^{-6}N(x)x$  represents additional phase shift as a change in effective path length  $\Delta x$ . This value is typically broken into two component parts [*Goldhirsch and Rowland*, 1982]:

$$\Delta x = (\Delta x)_{\text{dry}} + (\Delta x)_{\text{wet}} \quad (7)$$

where  $(\Delta x)_{\text{dry}}$  and  $(\Delta x)_{\text{wet}}$  represent the contributions to path length from the hydrostatic delay and from water vapor. Empirical measurement of these effects [*Smith and Weintraub*, 1953] shows that (7) may be approximated by

$$\Delta x = 7.76 \times 10^{-5} \int_0^x \frac{P}{T} dx + 3.73 \times 10^{-1} \int_0^x \frac{e}{T^2} dx \quad (8)$$

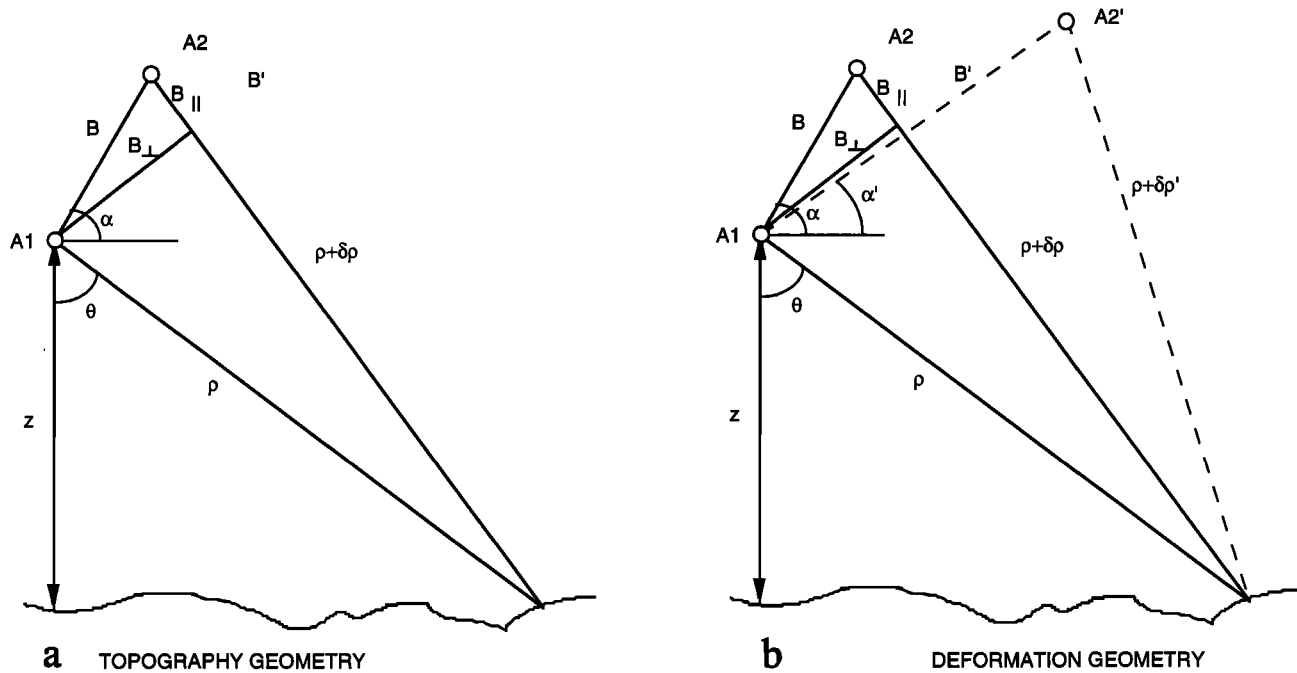


**Figure 1.** Interferometric imaging geometry interpretation relating (a) surface topography and (b) surface deformation to known platform parameters and measured radar distances. The height of the instrument above a point on the surface is  $z$ , the distance from the radar to that point is  $\rho$ , and the “look” angle is  $\theta$ . The interferometer configuration is given by the baseline length  $B$  and the baseline orientation angle with respect to horizontal  $\alpha$ . The baseline may be alternately described in terms of its components parallel to and perpendicular to the radar line of sight,  $B_{\parallel}$  and  $B_{\perp}$ . The extra distance traveled by the radar signal detected at the second antenna is  $\delta\rho$ , resulting in a phase shift proportional to this distance. Topography estimates follow from geometric solution for  $z$ . For deformation measurements a third, primed system may also be needed (Figure 1b), to remove ambiguity regarding whether the observed phase shift is due to topography or motion.

where  $X$  is the total path length through the atmosphere,  $P$  is the atmospheric pressure in millibars,  $T$  is the temperature in kelvins, and  $e$  is the partial pressure of water vapor in millibars. The constants preceding each integral are generally valid to within about 0.5% for frequencies up to 30 GHz and normal variations in pressure, temperature, and humidity.

The true path excess depends on detailed conditions of  $P$ ,  $T$ , and  $e$  along the propagation path from the radar sensor to the surface and back to the sensor. Since these quantities are not easily known for all points imaged in a radar swath, approximations in terms of surface parameters are often employed [Goldhirsh and Rowland, 1982]. Assuming models for the altitude dependence of pressure and temperature permits integration of (8) parameterized by the values of these quantities at the surface. For example, the Seasat radar altimeter team employed the following version of (8) expressed in terms of surface values [Jet Propulsion Laboratory, 1979; Saastamoinen, 1972]:

$$\Delta x = [2.277 \times 10^{-3} - 1.11 \times 10^{-5} \cos \Lambda]P, \\ + 2.277 \times 10^{-3} \left[ 0.05 + \frac{1255}{T_s} \right] e_s \quad (9)$$

where the subscripted values are the surface parameters and  $\Lambda$  is the latitude of the observation point.

The integration leading to (9) holds strictly only for an atmosphere whose pressure, temperature, and water vapor partial pressure vary with height smoothly according to the

assumed models. For the hydrostatic delay, for example, Saastamoinen [1972] assumes hydrostatic equilibrium. For the integration of the wet delay term a specific model in which temperature reduces with altitude at a constant lapse rate and in which the partial pressure of water vapor decreases exponentially is used. In addition, for nonnormal incidence a plane-parallel atmosphere is required. We will be examining cases where these quantities are distributed irregularly but assume that the deviations from average background values are small so that we may use the simplified model nonetheless.

Additional deviations from the simple propagation relationships used above affect the phase measurements, but the effects are small. The true ray path through the atmosphere is curved because of refraction, but here we can ignore the extra length due to curvature as we are interested only in the difference between the two curved paths illuminated by a radar sensor at different observation times. The differential curvature effects are negligible for the resolutions attained by today's spaceborne instrumentation. For nonnormal incidence an additional discrepancy arises: the models assumed in integration of (8) relate conditions along a vertical slice of the atmosphere, not an inclined slice along the radar incidence path. The actual values of  $P$  and  $T$  along the ray path are less well related to conditions at the surface reference point if the atmosphere possesses spatial variability. This complication aside, we can express the total additional two-way phase delay for side-looking imaging radars as

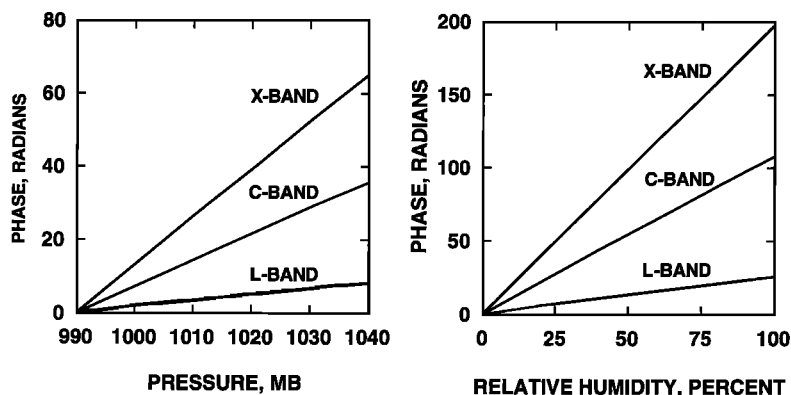


**Figure 2.** Excess atmospheric phase delay from pressure and humidity variations at each of the three SIR-C/X-SAR wavelengths. Total delay of up to 10 rad at L band (24 cm), 43 rad at C band, (5.7 cm), and 78 rad at X band (3.1 cm), relative to the value at 990 mbar, follows from variability in dry atmospheric pressure of 990 to 1040 mbar, about the normal annual range of mean pressures in the northern hemisphere. The phase delay due to the wet component of the troposphere ranges from 0 to 25 rad at L band for a humidity range of 0% to 100% and proportionately more at the shorter wavelengths. These values assume a nominal temperature of 300 K.

$$\Delta\phi = \frac{4\pi}{\lambda} \frac{\Delta x}{\cos\theta_i} \quad (10)$$

where  $\Delta\phi$  is the phase shift for the radar echo signal received from a point at incidence angle  $\theta_i$ . The maximum incidence angle  $\theta_i$  in data we use below is about  $60^\circ$ , resulting in an obliquity factor of 2.

As would be expected from our assumption that the atmosphere is nondispersive, that is,  $n(x)$  is real, equation (10) reflects strict proportionality of the phase with  $\lambda^{-1}$ , implying that multiple measurements at different frequencies will each infer the same delay expressed as a time value. Hence the delay cannot be determined by wavelength diverse measurements as is commonly done with ionospheric distortions. As we shall see below, the atmospheric delays cannot be separated from the phase signatures of either surface topography or deformation, since both produce equivalent distortions in the imaging geometry. Thus the expected value of these atmospheric effects must be considered in the interpretation of the observations.

In order to visualize the magnitude of the above effects, Figure 2 plots the integrated excess phase delay due to pressure and humidity variations from (10) at several wavelengths. Variability in dry atmospheric pressure ranging from 990 to 1040 mb, corresponding to the normal annual range of mean pressures in the northern hemisphere, produces a total excess phase delay of up to 10 rad at L band (24 cm wavelength), 43 rad at C band (5.7 cm wavelength), and 78 rad at X band (3.1 cm wavelength), relative to the value at 990 mbar. The phase delay due to the wet component of the troposphere ranges from 0 to 25 rad at L band for a humidity range of 0% to 100% and proportionately more at the shorter wavelengths. For Figure 2 we use a nominal temperature of 300 K. There also is a variation in phase due to temperature changes. For a nominal temperature of 273 K and 50% relative humidity, the L-band change is 10 rad for a 25 K temperature increase. It should be noted, however, that much of the temperature variation is due to partial pressure increases in water vapor that follow from keeping the humidity constant at 50%. For these illustrative cases we assume an incidence angle of  $45^\circ$ ; the effect will be more pronounced at more grazing incidence and less for incidence nearer normal.

### Interferogram Phase Measurements and the Atmosphere

The repeat-pass interferometric radar technique for derivation of surface topography or surface deformation follows from consideration of two radar systems observing the same ground swath from two positions A1 and A2, respectively, as illustrated in Figure 1a. Each radar independently measures the time delay for a signal transmitted from its antenna, to a point on the surface, and back to the radar. In a coherent radar the phase of each measured echo is exactly proportional to time delay, and the path difference of the two signals can be determined to subwavelength accuracy by observing the phase difference of the echoes.

If a resolution element on the ground scatters identically for each observation, then the difference of the two phases depends only on imaging geometry. If the two path lengths are taken to be  $\rho$  and  $\rho + \delta\rho$ , the measured phase difference  $\phi$  will be

$$\phi = \frac{4\pi}{\lambda} \delta\rho \quad (11)$$

or simply  $2\pi$  times the round-trip distance difference in wavelengths. If the distance to the scatterer  $\rho$  is much larger than the interferometer baseline  $B$ , the ray paths are approximately parallel so that

$$\delta\rho = B \sin(\theta - \alpha) \quad (12)$$

or

$$\delta\rho = B_{\parallel} \quad (13)$$

where  $B_{\parallel} = B \sin(\theta - \alpha)$  is simply the component of the baseline parallel to the look direction. This is the parallel-ray approximation used by Zebker and Goldstein [1986] in their initial paper on topographic mapping. Thus the measured phase of the interferometer is the component of the interferometer baseline parallel to the look direction to a given point on the surface measured in wavelengths, multiplied by two for round-trip travel. Inference of topography (denoted  $z$ ) follows from knowledge of the precise look angle  $\theta$  at each

point in the image from the relation  $z = h - \cos \theta$ ;  $h$  is the height of the instrument above a surface tangent plane.

For the surface deformation measurement, suppose further that a second interferogram is acquired over the same region as before, but in this case an earthquake has displaced each resolution element between observations (the primed interferogram in Figure 1b). The displacements are assumed small with respect to a resolution cell so that the radar echoes remain correlated. Here in addition to the phase dependence on geometry and topography there is a phase change due to the radar line-of-sight component of the displacement  $\Delta\rho$ . In this interferogram the phase  $\phi'$  will be given by

$$\phi' = \frac{4\pi}{\lambda} [B'_{\parallel} + \Delta\rho] \quad (14)$$

The displacement term  $\Delta\rho$  adds to the topographic phase term, yielding a sensitivity to subwavelength motion but creating confusion in the interpretation of the result. The phase in the radar interferogram depends both on the local topography (through  $B'_{\parallel}$ ) and also on any motion that may occur between viewing instances. In order to measure deformation unambiguously, the topographic term must be removed. This may be facilitated by independent knowledge of the topography, such as when a digital elevation model (DEM) of the area is available. Thus removal of topographic dependence is called the two-pass method, because only a single interferogram, made up of two radar passes, is required. Alternatively, the topography may be inferred from a second interferogram if it is known that no displacement of the surface occurred over its time interval. This approach, which does not require the independent DEM data, is called the three-pass method since at least three radar passes are needed to form the two interferograms.

Consider now interferogram formation using signals that have propagated through the atmosphere. The previous section describes how the phase of a single radar measurement is related to atmospheric conditions. In radar interferometry we combine two measurements of each surface point: the signal from the first complex radar image is multiplied by the conjugate of the signal in the second image, resulting in a total phase that is the difference of the two individual radar phases. This total phase is usually assumed to be related only to surface geophysical parameters such as topography or topographic deformation, and not to propagation effects in the medium. It is our purpose in this section to examine in more detail the effect of propagation delay variations on interferogram phase response.

Assume for the moment the absence of topography or deformation of the surface and that radar data are independently acquired by two antennas at nearly the same position in space. If there were no variation in atmospheric conditions between observations, or if the two radar images are acquired simultaneously, because the two rays experience the same round-trip echo delay the phase difference will be the "flat-Earth" interferometer fringe pattern. Thus, if the atmosphere is unchanging between observations in both pressure and humidity, even though the atmosphere contributes to the overall observed signal, the two atmospheric phase delays cancel out save for a very slight difference in path length resulting from a tiny change in incidence angle across the interferometer baseline. We can ignore this difference at present, it is a second-order path length correction in all of our observables. As long as the atmospheric state is unchanged between observations, the interferogram in this idealized case will be exactly the "flat-Earth" pattern. It follows that for the more realistic situation

where there are surface phenomena of interest, surface phase signatures will be uncontaminated by atmospheric propagation.

The phase delays due to the dry troposphere will change measurably if the air pressure changes at a given location between observation times. However, pressure variations with time at a given location are typically small in the absence of significant storm fronts. Typical rms variability values are 0.5–1.0 mbar in tropical regions, resulting from atmospheric tides, and 1–1.5 mbar in temperate regions, resulting from the movement of pressure centers [e.g., see *Ahrens*, 1994]. From (9), 1 mbar of pressure change leads to about 2.3 mm of delay change, much smaller than the water vapor variability we discuss below.

If the atmospheric pressure distribution is the same at both image acquisition times, each image will possess the same phase shift, dependent on topography since the total delay in the atmosphere depends on the thickness of the atmosphere "above" each point in the image. Even though the total dry tropospheric phase shift may be appreciable, it will be quite repeatable with time. Since in interferometry we measure phase differences, the net interferogram phase value is only that due to pressure changes with time and is usually small. For most topographic mapping applications, these elevation-dependent offsets in phase are typically ignored, and we will disregard them here. However, this correction may be important if very high accuracies over areas of extreme relief are required.

Unlike the dry tropospheric case, though, water vapor content is highly variable both spatially and temporally. The usual model assumed is that water vapor irregularities are "frozen into" the atmosphere and carried by the prevailing winds, generating both spatial and temporal variability [see, e.g., *Stull*, 1988; *Davis et al.*, 1993]. It is highly unlikely that on successive observations separated by days or weeks the water vapor distribution would remain constant, therefore significant phase residuals corresponding to as much as 30 cm of one-way delay are to be expected [*Goldhirsch and Rowland*, 1982]. Drier regions would have less variation, and wetter regions more.

Since the phase change due to atmospheric pressure change will likely be smaller than the residual expected from water vapor change, we will omit it in the following discussion. Instead, we focus on humidity effects and note that a parallel development concerning air pressure is quite similar.

### Effect on Topography and Surface Deformation Measurements

We can now estimate the effect of the variable atmosphere-induced phase errors on (1) repeat-pass topographic measurements, (2) two-pass surface deformation measurements, and (3) three-pass surface deformation measurements. We can consider the phase error values as given in Figure 2 as uncertainties in each radar image phase measurement. In the following sections the measurements of interferogram phase refer to the phase of the interferogram itself, not of each component radar image. It is important to recognize that in forming the interferogram two radar measurements are combined, therefore the standard deviation of the interferogram phase will be  $\sqrt{2}$  times the standard deviation of each radar measurement, given that they are of equal average magnitude to begin with. The individual radar echoes from distributed targets have random phases, which are in turn modified by propagation effects, and are not easily determined before the interferogram differ-

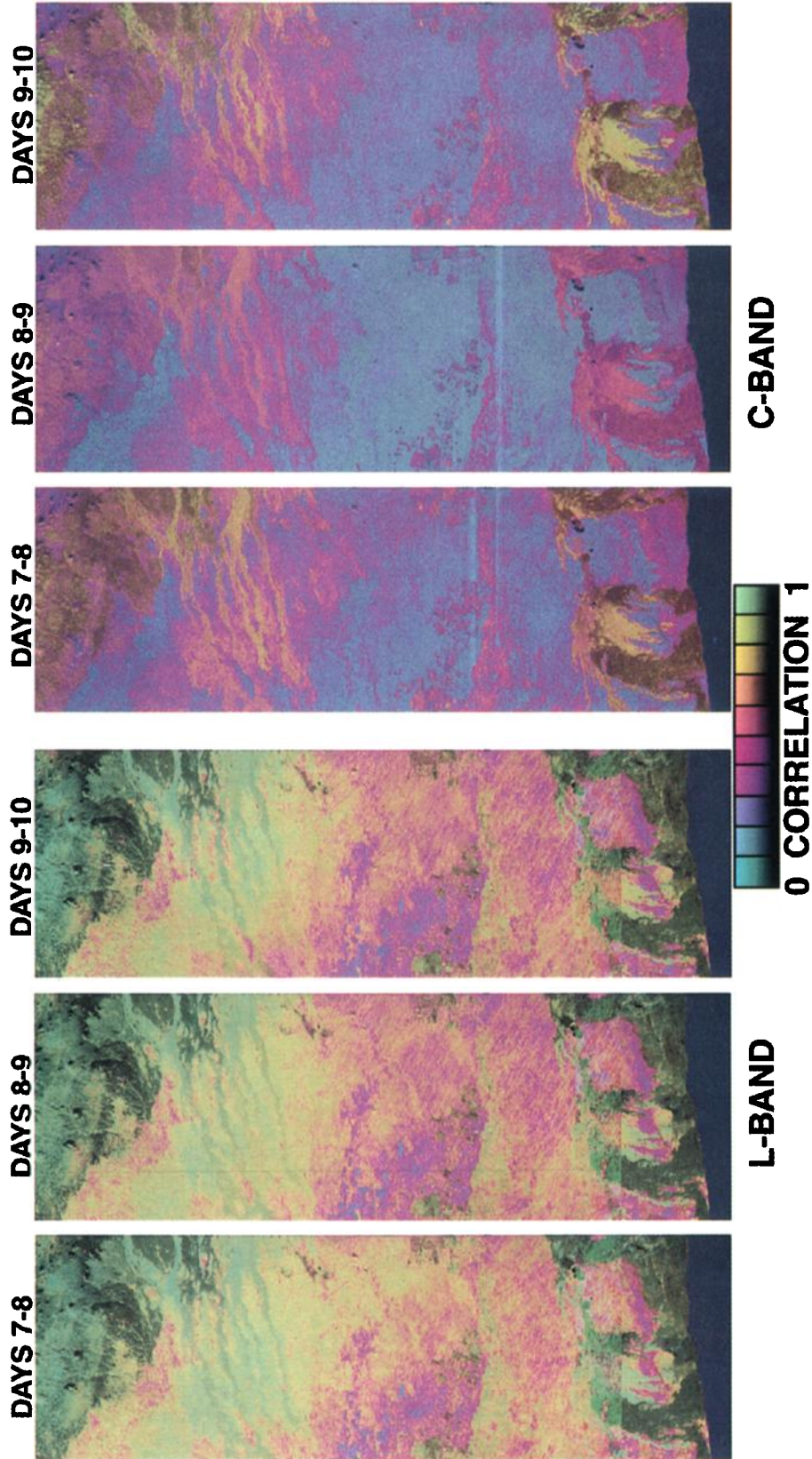


**Plate 1.** L band and C band correlation images. Correlation at L band exceeds that at C band, sometimes greatly. The sequence of L band images shows correlation becoming steadily weaker with time, with the rate dependent on surface terrain. The rate is slowest on the bare lava regions and fastest in the vegetated areas. For C band the observed correlation changes abruptly from day to day, sometimes increasing, sometimes decreasing.

ence is generated. Thus we will use the interferogram phase as our basic measurement.

Height error as a function of phase error for topographic analysis is given by *Zebker and Goldstein* [1986] or *Rodriguez and Martin* [1992], who obtain the following expression by differentiating the topographic phase relation of the interferometer with respect to the measured phase  $\phi$ :

$$\sigma_z = \frac{\lambda \rho}{4\pi B} \frac{\sin \theta}{\cos(\theta - \alpha)} \sigma_\phi \quad (15)$$

where  $\theta$  is the look angle,  $\alpha$  is the interferometer baseline orientation with respect to horizontal,  $\sigma_\phi$  is the phase error in the interferogram, and  $\sigma_z$  is the resultant height error. Using the estimates for propagation variations obtained above and equation (15), we can describe the height errors in repeat pass measurements as a function of the geometry and of the atmospheric variability.

Figure 3 plots the error in estimated heights as a function of the change in water vapor between observations. These values are plotted for baseline lengths of 100, 200, and 400 m and assume nominal imaging parameters of 45° incidence, a range of 300 km, and a horizontal baseline (equal spacecraft height at both observations). Note that even modest changes in relative humidity of 20% cause over 290 m of topographic error for the 100 m baseline system, independent of wavelength due to the  $\lambda$  dependence of (15). As shown in Figure 3, the errors are proportionally smaller for the longer baseline lengths. These errors are unacceptably large for most systems as the resulting data would be of similar or poorer quality to those in existing data bases.

Now we consider cases 2 and 3 above, the two-pass and three-pass surface deformation measurements. Here the interferogram phase is either corrected for expected topographic variation as calculated from an independently derived digital elevation model [*Massonnet et al.*, 1993], or else three passes are used to separate the topographic and deformation signatures. The deformation error  $\sigma_\rho$  for case 2 is easily derived from the linear relationship between displacement and range [*Zebker et al.*, 1994b] and is given by

$$\sigma_\rho = \frac{\lambda}{4\pi} \sigma_\phi \quad (16)$$

In practice, DEMs have inaccuracies that often are the principal error sources in the derived deformation maps. The noise from the DEM uncertainty may be derived using the inverse of (15) and applying that effective phase noise to the deformation error in (16). As a numerical example, a DEM with 10 m errors generates an effective phase noise of about 0.25 rads, if an L band radar is at 300 km range, pointed 45° off nadir, and has a 100 m baseline perpendicular to the line of sight. This phase noise then corresponds to a deformation error of approximately 0.5 cm from (16).

In case 3 we derive the corresponding error from the linearized expression for the inferred change in range as a function of the two interferogram phases measured at each point [*Gabriel et al.*, 1989; *Zebker et al.*, 1994b]:

$$\Delta \rho = \frac{\lambda}{4\pi} \left( \phi_d - \frac{B_d}{B_t} \phi_t \right) \quad (17)$$

where the line-of-sight baseline component of the “topographic” pair of the differential interferogram triplet is  $B_t$ , the line-

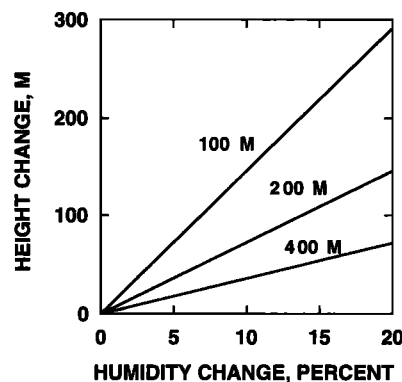


**Figure 3.** Error in inferred topography as a function of the change in water vapor between observations for any of the three SIR-C/X-SAR wavelengths. Curves correspond to baseline lengths of 100, 200, and 400 m and assume nominal imaging parameters of 45° incidence, a range of 300 km, and a horizontal baseline. Even modest changes in relative humidity of 20% cause over 290 m of topographic error for the 100 m baseline system, independent of wavelength. The errors are proportionally smaller for the longer baseline lengths.

of-sight baseline component of the “deformation” pair is  $B_d$ ,  $\Delta \rho$  is the measured deformation, and  $\phi_d$  and  $\phi_t$  are the “deformation” interferogram and “topographic” interferogram phase observations, respectively. In the three-pass method the interferogram differences  $\phi_d$  and  $\phi_t$  share a single common phase from the shared antenna differenced with two additional phase values from the two other antennas, resulting in a covariance matrix of the form

$$\Lambda_\phi = \begin{bmatrix} \sigma_\phi & \frac{1}{2} \sigma_\phi \\ \frac{1}{2} \sigma_\phi & \sigma_\phi \end{bmatrix} \quad (18)$$

The phases are not independent because of the shared measurement. Assuming standard deviation  $\sigma_\phi$  on each interferogram phase measurement, we obtain an error in the deformation  $\sigma_\rho$  of

$$\sigma_\rho = \frac{\lambda}{4\pi} \sqrt{1 - \frac{B_d}{B_t} + \frac{B_d^2}{B_t^2}} \sigma_\phi \quad (19)$$

The uncertainty of the deformation measurement here is dependent on the relative baseline lengths since the third radar pass is used to generate the topographic correction directly, rather than using an additional independent DEM, and statistical variation in the third phase measurement adds to the total error.

The error from (16) and (19) due to atmospheric water vapor variations is plotted in Figure 4. For two-pass deformation measurements the error is independent of both baseline and wavelength, whereas for three-pass implementations the error is similar in magnitude but depends somewhat on the ratio of the two baselines. Our plot assumes equal line-of-sight baseline lengths, and thus the error is  $\sqrt{2}$  times the two-pass result. We note again unacceptably high errors: the two-pass case error is nearly 10 cm and the three-pass case error is nearly 14 cm for humidity variations of 20%. This is not helpful in a technique aimed at centimeter-level deformation mapping.

Another implementation of the deformation measurement uses four passes, rather than two or three. In this instance, two passes form a topographic estimate, and that topography esti-

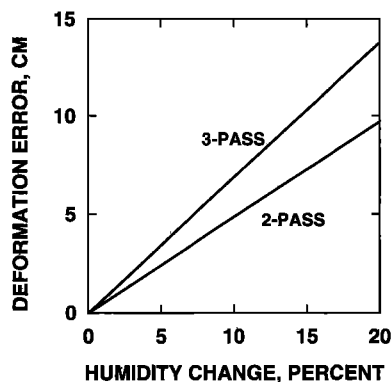


**Figure 4.** Error due to atmospheric water vapor variations in two- and three-pass deformation measurements. In the two-pass case the error is independent of both baseline and wavelength, whereas for three-pass implementations the error is similar in magnitude but depends somewhat on the ratio of the two baselines. The two-pass case error is nearly 10 cm and the three-pass case error is nearly 14 cm for humidity variations of 20%.

mate is used to remove the topographic signature from an interferogram with both motion and height contributions. The advantage of this implementation over the three-pass case is that only the two pairs of images forming the interferograms need to be analyzed coherently, so that temporal decorrelation effects are lessened. The errors in this implementation follow from using parameters of the topographic pair to generate height error estimates from (15), and these height errors would be applied to the inverse of (15) using the parameters of the deformation pair. The net result, if the imaging geometry of the two pairs is similar, is that the phase errors in the topographic pair are scaled by the ratio of the perpendicular baseline components of the two pairs. Depending on which pair has a greater baseline, the phase errors in the topographic interferometric pair may be increased or diminished. The resulting effective phase noise once again is used in (16) to get deformation error estimates as above.

In summary, large variations in atmospheric water vapor content can compromise the effectiveness of interferometric techniques for both the measurement of topography and surface determination from space. In the next section we will examine actual measurements to analyze the utility of spaceborne interferometric radar measurements that may be limited by such variations.

## Observational Data

From April 9–20 and again from September 30 to October 11, 1994, the Space Radar Laboratory (SRL) aboard the space shuttle *Endeavor* mapped the surface of the Earth with a multiparameter imaging radar system. SRL instrumentation includes SIR-C, a dual frequency, four polarization radar, plus the single frequency and polarization X-SAR radar, permitting simultaneous radar data acquisition at up to three wavelengths. This imaging radar suite measured the complex surface backscatter intensity and phase at nominal 5 m spatial resolution over 20–50 km wide by several hundred kilometer long radar swaths.

Two different geometries afforded interferometric application of SRL data. Orbital tracks from day 4 of the first mission

(SRL-1) were repeated nearly exactly on day 4 of the second mission (SRL-2), thus complex images from the two missions separated in time by 6 months can be compared for interferometric phase signatures. In addition, days 7–10 of the SRL-2 mission each consisted of the same set of ground tracks, permitting the formation of interferograms with 1-, 2-, and 3-day temporal baselines. Because the repeatability of shuttle orbit tracks at the precision required for radar interferometry was untested before the SRL flights, the NASA mission planners used a conservative approach: they attempted to fly the repeat orbits with zero baseline, aiming for exact repeats. As it happened, shuttle engineers were very nearly able to achieve exactly repeating orbits, with many orbits less than 200 m from their respective interferometric partners. As we shall see below, this has the unfortunate consequence of limiting the usefulness of these data for topographic mapping purposes. Table 1 summarizes the main characteristics of the SRL instrumentation.

While there have been demonstrations of interferometric techniques using data acquired by X-SAR also [Moreira *et al.*, 1995], we present SIR-C data only here for three reasons: (1) the data were more readily available to us, (2) relaxed baseline requirements at the longer SIR-C wavelengths made product generation simpler, and (3) the C and L band wavelengths suffice for demonstrating wavelength dependence. We also use here data only from the day-scale temporal baselines, as the 6-month data have been described previously [Rosen *et al.*, 1996], and the shorter time-baseline data exhibit the desired atmospheric variation without involving longer timescale decorrelation and motion effects.

We present here interferometric reductions of data acquired over Kilauea, Hawaii. Data were acquired on 4 successive days, from October 7 through 10, 1994. By coincidence these correspond to days 7–10 of the SRL-2 mission, counting the launch day as day 0. These are the exact-repeat orbit days; that is, the shuttle covered the same set of ground tracks on each day. We processed the L band and C band passes for each of these and formed interferograms of 1-, 2-, and 3-day temporal baselines using data from days 7–8, 7–9, and 7–10, respectively. We also processed the two additional 1-day baseline pairs, from days 8–9 and 9–10.

Figure 5 is a shaded relief representation of the island of Hawaii with the SRL imaged swath overlaid. The processed track extends from an area containing cinder cones located near the top of Mauna Kea, down through the then active regions along the Chain of Craters, and finally to the Pacific Ocean. Also shown are four locations, denoted A, B, C, and D,

**Table 1.** Nominal SIR-C/X-SAR System Parameters for Interferometric Modes

Radar Parameter	L Band	C Band	X Band
Frequency, GHz	1.240	5.285	9.603
Maximum range bandwidth, MHz	40	40	20
Peak transmit power, W	6000	3000	3000
System noise temperature, K	1100	1300	1500
Pulse repetition rate	1250–1850	1250–1850	1250–1850
Antenna dimensions, m	12 × 2.9	12 × 0.7	12 × 0.4
Antenna elevation beamwidth	5°	5°	5.6°
Critical baseline length, m	8000	1870	515
Satellite altitude, km	205	205	205
Maximum look angle	55°	55°	55°
Ground range swath, km	20–50	20–50	20–50

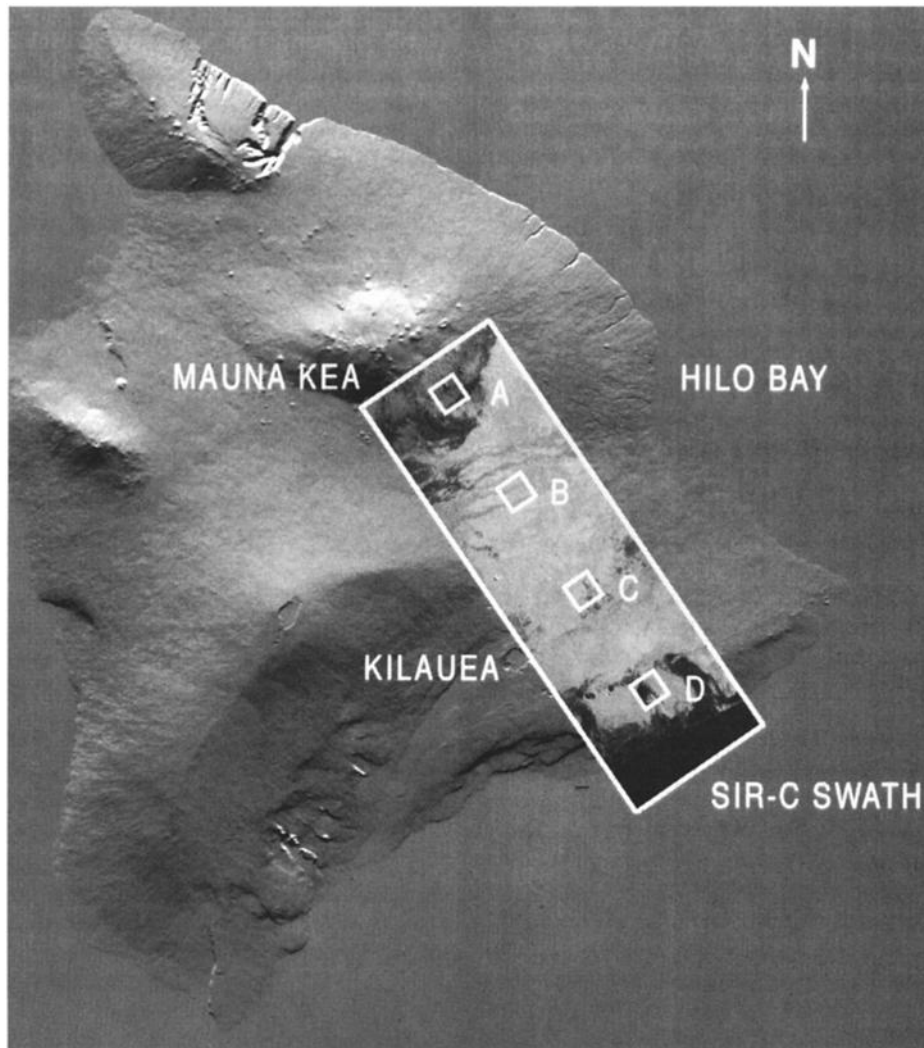


**Figure 5.** Area imaged in our exact-repeat swaths is a portion of the Big Island of Hawaii, the SIR-C/X-SAR imaged swath is overlaid. The processed track extends from an area containing cinder cones located near the top of Mauna Kea, down through the then active regions along the Chain of Craters, and finally to the Pacific Ocean. Also shown are four locations, denoted A, B, C, and D, arbitrarily chosen for detailed quantitative comparisons of phase and height errors.

arbitrarily chosen for detailed quantitative comparisons of phase and height errors. This same swath was imaged on the four exact-repeat days within about 200 m.

Correlation images, in which we plot the brightness at each pixel proportional to radar signal strength and color by its correlation in the interferogram, for each of the SIR-C swaths are shown in Plate 1. Several characteristics of the correlation values are immediately apparent. First, as has been noted theoretically many times [e.g., see *Li and Goldstein, 1990; Rodriguez and Martin, 1992; Zebker and Villasenor, 1992; Zebker et al., 1994c*] and observationally by *Rosen et al. [1996]*, the correlation at the longer wavelengths generally exceeds that at the shorter wavelengths, sometimes greatly. Also, examining the 1-, 2-, and 3-day sequence of L band correlation images shows that at this wavelength the correlation gets steadily weaker with time, with the rate dependent on surface terrain. The rate is slowest on the bare lava regions and fastest in the vegetated areas. This observation corresponds with the previous study of *Zebker and Villasenor [1992]*, which was also conducted at L band.

A different conclusion results from examination of the C-band data for the same sequence. Here, the correlation changes abruptly from day to day, sometimes increasing, sometimes decreasing. A similar effect was noted by *Zebker et al. [1994a]* from data acquired over Toolik Lake in Alaska by the ERS-1 satellite, a C band system. In that case the nonuniform change was found to correspond to freezing and thawing of the ground surface, resulting in different scattering mechanisms for each state and consequential decorrelation.

Clearly, the scattering behavior and decorrelation causative mechanisms of the Kilauea surface at the two wavelengths is quite different and not simply related by scaling of the surface roughness. We can explain the C band correlation observations if the surface is being altered on the size scale of the shorter wavelength (6 cm) in a reversible way, otherwise the correlation on the days 7–10 interferogram would not exceed that on days 7–9 and 7–8. One possibility here is accumulation of water in centimeter-sized pockets in the lava and in the soil, which can modify the structural details of the surface/air interface, and later dry out to return the surface to its initial state.

**Table 2.** Estimated Interferometric Baselines

Orbit Pair	$B_{\text{perp}}$ , m	$B_{\text{par}}$ , m	Residual Phase Error, rad
Days 7–8	199.1	178.1	1.08
Days 7–9	–100.6	–53.7	0.82
Days 7–10	56.3	108.3	0.81
Days 8–9	–300.3	–236.2	0.92
Days 9–10	156.9	157.6	0.72

$B_{\text{perp}}$  is component of interferometer baseline perpendicular to line of sight and  $B_{\text{par}}$  is component of interferometer baseline parallel to line of sight.

Water drops on the vegetation could have a similar effect, though both of these speculations are as yet unproven. This remains a topic for future study that is important for any application of repeat-pass interferometric techniques.

Spaceborne observations will also be corrupted by ionospheric propagation, leading to phase shifts, scintillation, and Faraday rotation effects that are worse at longer wavelengths. While beyond the scope of this paper, these phenomena will set a lower bound on the frequency selection for interferometric radar design.

Now we estimate the atmospheric variation effect in these data sets, expressed as a phase residual in each of the L band interferometric pairs. The residual is obtained by subtracting a theoretical topographic phase signature, derived from knowledge of the imaging geometry and a digital elevation model of the surface, from the observation. This is the two-pass technique used by *Massonet et al.* [1993, 1994], for example, in order to separate the topographic signature from the deformation effects. In order to calculate the expected phase variations due to topography, the imaging geometry is described by shuttle orbital parameters and high-precision estimates of the interferometric baseline. Since the shuttle orbit is not known well enough to solve for the baseline from orbital information alone, a procedure for estimating the orbit given the interferometer response itself is required. Hence we derive the baseline from a least squares fitting procedure where the measured phases as a function of baseline parameters are compared to predicted phases at reference tie points of known elevation. This procedure is described in some detail in an appendix of *Rosen et al.* [1996]. Once the imaging geometry is determined, we calculate the expected topographic phase response of each interferogram pair and subtract it from the observations, resulting in a topographically “corrected” interferogram. If the model of propagation and surface scatter were perfect, the resulting interferogram would have uniformly zero phase.

The inferred baselines for the Kilauea data are shown in Table 2, which lists components of the interferometer baseline perpendicular and parallel to the radar line of sight, as well as the residual phase from the solution. The known reference elevations are those in the U.S. Geological Survey (USGS) digital elevation model of the area. For these solutions we used hundreds of thousands of tie points, one for each of the available DEM locations. Since the orbits are not perfectly parallel, we solve for both baseline components at the swath starting point, as well as convergence rates for each component with time and an overall offset phase. These convergence rates are not included in Table 2.

Interferograms which have been corrected for known topography are shown in Plate 2. The images are far from uniform

and are noisier at C band than at L band by the ratio of the imaging wavelengths, as would be expected if atmospheric effects dominate (see previous section). That the phase signature is related to the atmosphere is likely because of several points: (1) the ratio of the phase artifact level in the images is the wavelength ratio, (2) the phase irregularities are unrelated to surface features, so that they are probably not surface scattering changes, (3) they are different from day to day, whereas surface-induced changes should be spatially correlated in different data sets, and (4) the effect is most pronounced at lower elevations, where the ray path through the atmosphere is longest and thus most sensitive to variation in an absolute sense.

Examination of the 1-day sequence of pairs 7–8, 8–9, and 9–10 shows several irregularities that appear on two successive interferograms, but with opposite sign, such as the crescent-shaped object one third of the way down the 7–8 and 8–9 images. This is easily understood as a “blob” of water vapor present on day 8. Since the interferograms here are all formed by subtracting the phase of the later image from that of the earlier image, the phase of the irregularity is negative in the day 7–8 interferogram and positive in the day 8–9 interferogram.

We list the magnitude of the phase variation in Table 3 as rms phase variation in radians for the topographically corrected L band interferograms at each of four locations, located progressively from Mauna Kea, to the Chain of Craters area, and to the ocean. The residuals agree approximately in magnitude with the average residuals found in the baseline estimation process (see Table 2).

A final clue that these variations are due to atmospheric water vapor is derived by examining estimates of tropospheric delay derived from Global Positioning Satellite (GPS) system receivers operating simultaneously with our observation period in Hawaii. In Figure 6 we plot data acquired from the UWEK GPS location, near Kilauea, consisting of the difference of the estimated zenith path delays between measurements spaced 1 day apart, equivalent to our 1-day baselines. We show the 1-day differences for periods beginning during the interval from midnight October 7 through midnight October 9. This GPS “error” is usually recognized as unmodeled variable atmospheric water vapor. The left-hand scale gives the differences in centimeters of the estimated one-way travel vertical change, while the right-hand scale expresses the differences in equivalent L band two-way slant range radar phases as shown in Table 3. This plot represents data for only one spot near the Kilauea crater, but the approximate agreement in magnitudes again leads us to conclude that the observed radar distortions and artifacts are due to water vapor.

For the Hawaii data the phase standard deviations are up to an order of magnitude higher than the values *Goldstein* [1995] reported in the California desert. This should be expected if the water distribution is a turbulent process that distributes the more plentiful water vapor present in the Hawaiian atmosphere. These empirically observed phase errors affect geophysical products derived using interferometric techniques as follows.

### Derived Geophysical Products: Topography and Deformation Maps

In this section we generate sample topographic and deformation products using the L band Hawaii data to minimize decorrelation effects and to examine the inaccuracies in them resulting from the variability in the atmosphere. The C band

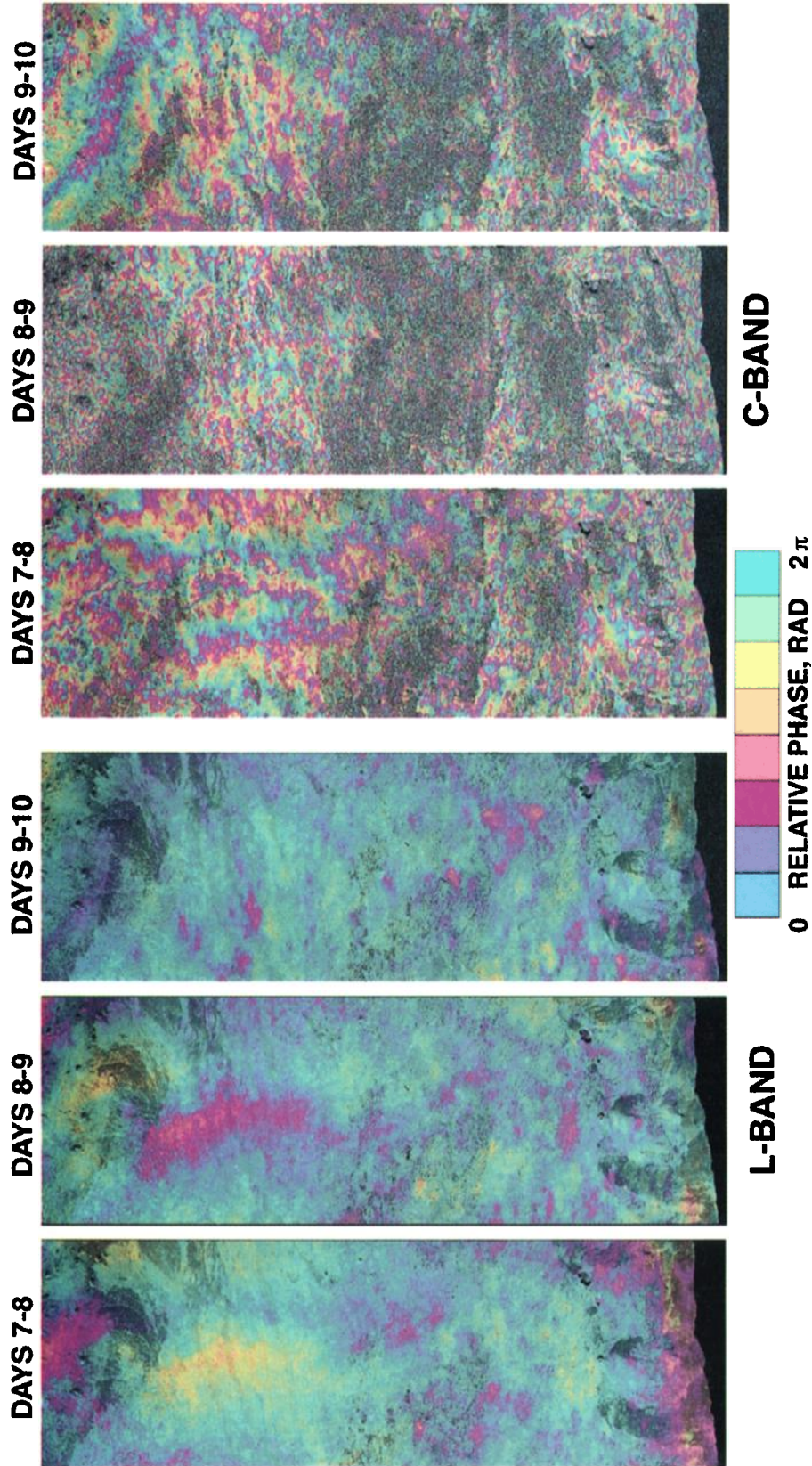


**Plate 2.** Interferograms corrected for known topography show atmospheric artifacts clearly. Not only are the C band images subject to severe decorrelation, but they are noisier by the ratio of the imaging wavelengths than the L-band images. This is one indication that atmospheric effects dominate.

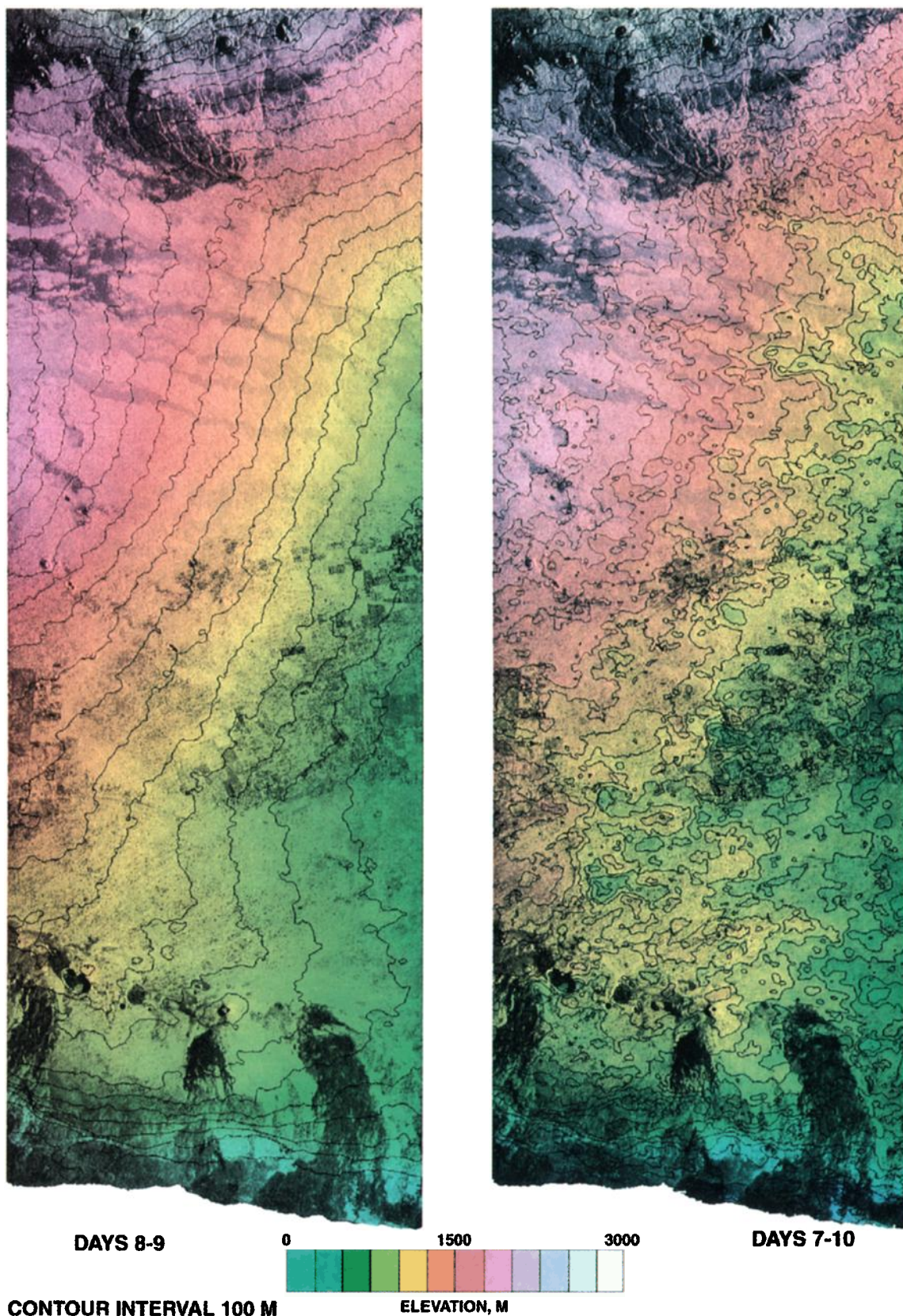


**Plate 3.** DEMs derived from two interferometric baseline pairs illustrate that topographic errors can be decreased if a longer baseline pair is used. The days 8–9 pair has a baseline of 300 m, while for days 7–10 the baseline is only 56 m. Images show radar backscatter maps color coded with height, as well as 100 m spaced contour lines. The days 8–9 pair easily supports contouring at this level, while the 7–10 pair is highly contaminated with spurious contours from the atmospheric variations.

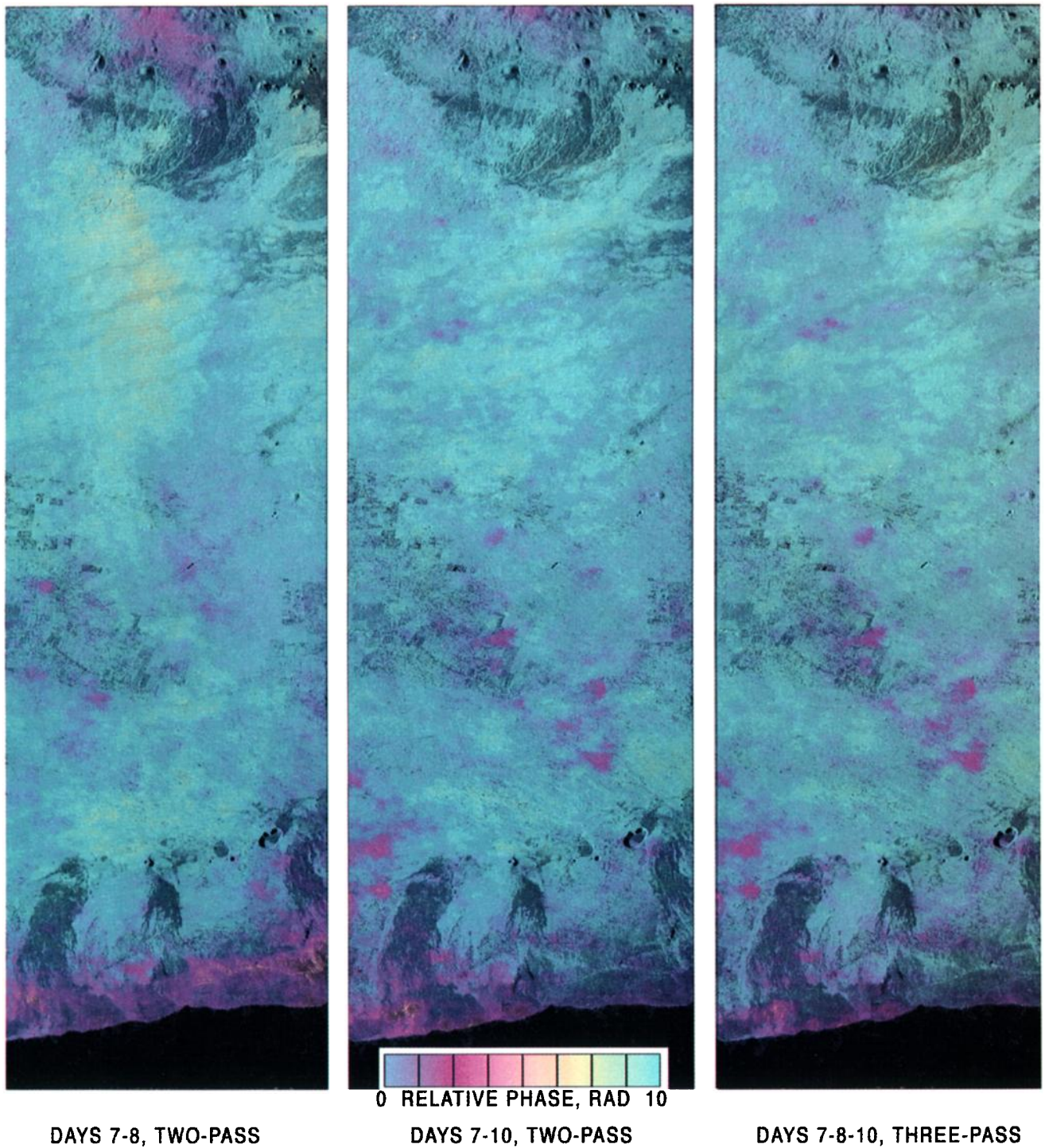


**Plate 4.** Artifacts in several L band deformation data products. Similar levels of atmospheric contamination are seen in both two- and three-pass deformation implementations.



**Plate 5.** Two-pass differential interferograms derived from data acquired on days 7–8 and on days 9–10, along with the average of the two. Whereas in topographic mapping the errors are dependent on baseline parameters, the surface deformation is independent of (two-pass case), or depends only weakly on (three-pass case), the baseline. However, averaging of measurements obtained from completely independent pairs reduces noise. Statistically, if the noise level in two images is the same, their average will have less noise by a factor  $\sqrt{2}$ .

**Table 3.** L Band rms Phase Measurements

Location	Oct. 7-8	Oct. 8-9	Oct. 9-10	Oct. 7-9	Oct. 7-10
A	0.66	0.46	0.34	0.39	0.23
B	0.32	0.28	0.50	0.27	0.39
C	0.53	0.54	1.00	0.43	0.93
D	0.50	0.64	0.58	0.81	0.52

In radians.

data would exhibit identical errors from propagation delay but be further corrupted by additional decorrelation noise. First, we discuss the topographic case, and then we look at deformation measurements.

For a given phase error the topographic elevation error is inversely dependent on the perpendicular component of the baseline (see equation (11)). Thus, given a set of possible interferometric image pairs in the presence of noise, we should use the pair with the greatest perpendicular baseline. The baselines for the Kilauea data were shown in Table 2. The days 7-10 pair possesses the smallest perpendicular baseline and could be expected to yield the poorest elevation model, while the pair from days 8-9 should yield the highest quality product.

In Plate 3 we show image DEMs, consisting of radar backscatter maps color coded with height, as well as 100 m spaced contour lines. The days 8-9 pair easily supports contouring at this level, while the 7-10 pair is highly contaminated with spurious contours from the atmospheric variations. To obtain an initial estimate of the quality of the DEM from these pass pairs, we compute the worst case order unity standard deviation of the phase in radians observed in the topographically corrected interferograms (see Table 3). From (11) we find that the expected maximum elevation errors for these two DEM

reconstructions are 117 m and 22 m, for the days 7-10 and days 8-9 elevation models, respectively.

To illustrate a more precise evaluation of the performance of the SIR-C radar as a topographic mapping instrument, we compare the inferred elevations with independently derived data. Since we have the topographic data from the USGS available, we can evaluate the actual errors in the DEM reconstructions and compare to the predicted errors we obtain from the phase defect measurements. In Table 4 we list the rms phase errors, predicted rms elevation errors, and measured rms elevation errors for several regions in the two digital elevation models. The predictions are obtained using (11). The predicted and measured errors agree within about 10%, as expected since the same reference DEM was used both in the phase defect determination and in the height error measurement. The comparison is somewhat tautological but shows the values that characterize the accuracy of the instrument for topographic applications can be expressed either as phase or height errors.

We next consider the accuracy of deformation maps of Kilauea produced by SIR-C using both the two- and three-pass methods. Sample phase defect images shown in Plates 4a and 4b represent the two-pass deformation products directly, once the phase measurements have been converted to distance by simple scaling by  $\lambda/4\pi$ .

The two-pass products discussed above require that an independent DEM of the area be known. In the event of unavailability of such a DEM, we can instead generate a three-pass deformation map that does not require a DEM. It does require some knowledge of the interferometer baseline, however, obtained for example from orbital information, pixel offsets in the radar images, or ground control points. We illustrate in Plate 4c a three-pass differential interferogram of Kilauea

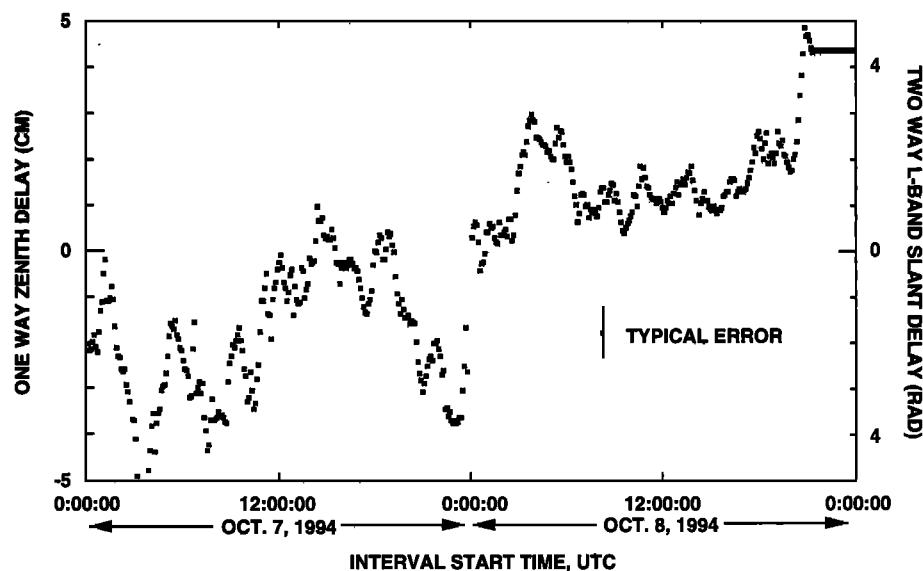


**Figure 6.** Data acquired from the UWEK GPS location near Kilauea crater consisting of the difference of the estimated path between measurements spaced 1 day apart, equivalent to our 1-day baselines. This graph gives the 1-day GPS estimated zenith path differences for periods beginning during the interval from midnight October 7 through midnight October 9, and thus ending 24 hours later on October 8 and 9, 1994. This provides another clue that these variations are due to atmospheric water vapor. This GPS “error” is usually recognized as unmodeled variable atmospheric water vapor. The left-hand scale gives the differences in centimeters of the estimated one-way travel vertical change, while the right-hand scale expresses the differences in equivalent two-way L band slant range radar phases.

**Table 4.** L Band RMS Phase and DEM Errors

Location	Days 7–10			Days 8–9		
	RMS Phase, rad	Predicted, m	Measured, m	RMS Phase, rad	Predicted, m	Measured, m
A	0.23	26.8	30.8	0.46	10.1	10.9
B	0.39	45.5	40.9	0.28	6.1	6.6
C	0.93	108.5	110.6	0.54	11.8	12.5
D	0.52	60.7	60.3	0.64	14.0	14.9

derived from data acquired on days 7, 8, and 10 of the second SIR-C mission, the same data as were used in generation of the two-pass deformation maps in Plates 4a and 4b. In Table 5 we summarize the error in centimeters of two- and three-pass deformation measurements. These values are the standard deviations of the measured phases, and the peak errors detected will be, of course, several times these.

In the earlier example of topography mapping, the errors were seen to be mitigated somewhat by judicious selection of interferometric pairs dependent on baseline parameters. However, as can be seen in (12) and (15), the surface deformation is independent of (two-pass case), or depends only weakly on (three-pass case), the baseline. Thus choosing interferometric pairs according to baseline information will not significantly help to reduce the effect of the atmospheric noise in the deformation products. Instead, we can use simple averaging of the measurements obtained from completely independent pairs to reduce the noise. This approach to noise reduction is illustrated in Plate 5, where we plot two-pass differential interferograms derived from data acquired on days 7–8 and on days 9–10, along with the average of the two. Note that the overall noise level is smaller and that although atmospheric features present in both of the initial interferograms can be seen in the average interferogram, their amplitude is lessened. Statistically, if the noise level in two images is the same, their average will have less noise by a factor  $\sqrt{2}$ . We note that combining two deformation pairs with similar noise levels, within a factor of 3 in amplitude, the resulting average image will have improved noise quality than either of the original images. We tabulate the reduction in phase noise in Table 6.

## Conclusions

We have seen that interferogram images derived from repeat pass spaceborne synthetic aperture radar systems exhibit artifacts due to the time and space variations of atmospheric water vapor. Other tropospheric variations, such as pressure and temperature, also might be expected to induce distortions, but the effects are smaller in magnitude and more evenly distributed throughout the interferogram than the wet troposphere term. Spatial and temporal changes of 20% in relative

humidity lead to 10 cm errors in deformation products and perhaps 100 m of error in derived topographic maps for those pass pairs with unfavorable baseline geometries. In wet regions such as Hawaii, these errors are by far the dominant ones in the SIR-C/XSAR interferometric products.

We noted first that the correlation observed was significantly greater at the longer, L band wavelength of SIR-C than at the C band wavelength. In addition, since the atmospheric delay in centimeters is independent of wavelength for a system that is limited by these effects the most accurate results will derive from the highest correlation interferograms, indicating that the longer L band measurements are preferred. Of course, if other wavelength-dependent scattering phenomena are the object of the study, the shorter C band may be desired.

Again, since the dominant error effect is due to propagation in a neutral atmosphere, the magnitude of the phase distortion scales with frequency, and thus multiwavelength measurements, such as those commonly used to correct radar altimeter and GPS measurements, cannot be used. In the topographic case the errors may be mitigated by choosing interferometric pairs with relatively long baselines, as the error amplitude is inversely proportional to the perpendicular component of the interferometer baseline. For the Hawaii data we found that the best (longest) baseline pair produced a map supporting contouring at the 100 m level, whereas the poorest baseline choice yielded an extremely noisy topographic map even at this coarse contour interval. The baseline chosen must still conform to the critical baseline criterion for baseline decorrelation, however.

In the case of deformation map errors the result is either independent of baseline parameters or else very nearly so. Here the only solution is averaging of independent interferograms, so in order to create accurate deformation products in wet regions many multiple passes may be required.

While it is possible to remove some of the water vapor effects in the radar interferograms if we have access to water vapor radiometer or GPS estimates of the wet tropospheric content, this is generally impractical for several reasons. As seen in the images presented above, the water vapor irregularities occur on many size scales, down to 100 m or less. Similar size scales are inferred from the power spectrum determined by *Goldstein* [1995] in his Fort Irwin, California, measurements. GPS methods for sensing integrated water va-

**Table 5.** Two- and Three-Pass RMS Deformation Errors

Location	Days 7–8, Two Pass	Days 7–10, Two Pass	Days 7–8–10, Three Pass
A	1.2	0.4	0.4
B	0.6	0.7	0.8
C	1.0	1.8	1.7
D	1.0	1.0	0.9

In centimeters.

**Table 6.** L Band rms Phase Error

Location	Days 7–8	Days 9–10	Average
A	0.66	0.34	0.29
B	0.32	0.50	0.28
C	0.53	0.96	0.55
D	0.50	0.58	0.30

por are one possibility for artifact compensation [Rocken *et al.*, 1993]; however, the GPS receiver ground density would have to be at 100 m or better spacing in both dimensions to remove the spurious signal fully, clearly an impractical situation. Water vapor radiometers, another source for correction data, do not yet achieve such fine resolution from space platforms, which would be required to supplement the global coverage offered by the radar system. Local, coordinated aircraft underflights of the satellites using high-resolution instrumentation could in principle determine the corrections, but precise temporal coordination with the radar satellite is difficult, and in any case this approach eliminates the one great advantage of spaceborne radar topographic and deformation systems, that of global and synoptic coverage. Future technological developments may, however, enable these approaches.

Therefore we can state the following rules for increasing the accuracy of geophysical data products derived from interferometric analysis in nondesert parts of the world: (1) use the longest radar wavelengths possible, within ionospheric scintillation and Faraday rotation limits, (2) for topography, maximize interferometer baseline within decorrelation limits, and (3) for surface deformation, use multiple observations and average the derived products.

Following the above recipe yields 10 m DEM accuracy and 1 cm deformation accuracy even in very wet regions, such as Hawaii. These performance values should be sufficient to support many interesting interferometric experiments.

**Acknowledgments.** We would like to acknowledge the NASA JPL Spaceborne Imaging Radar Team for great effort over many years to make these data available. We would also like to thank our reviewers and Associate Editor for many useful comments leading to improvements of the manuscript. This work was supported by the NASA SIR-C project and by the NASA Topography and Surface Change Program.

## References

- Ahrens, C. D., *Meteorology Today*, 5th ed., West Publ., Minneapolis/St. Paul, Minn., 1994.
- Davis, J. L., G. Elgered, A. E. Niell, and C. E. Kuehn, Ground-based measurement of gradients in the "wet" radio refractivity of air *Radio Sci.*, 28(6), 1003–1018, 1993.
- Gabriel, A. K., R. M. Goldstein, and H. A. Zebker, Mapping small elevation changes over large areas: Differential radar interferometry, *J. Geophys. Res.*, 94(B7), 9183–9191, 1989.
- Goldhirsh, J., and J. R. Rowland, A tutorial assessment of atmospheric height uncertainties for high-precision satellite altimeter missions to monitor ocean currents, *IEEE Trans. Geosci. Remote Sens.*, GE-20(4), 418–433, 1982.
- Goldstein, R., Atmospheric limitations to repeat-track radar interferometry, *Geophys. Res. Lett.*, 22(18), 2517–2520, 1995.
- Goldstein, R. M., H. Engelhardt, B. Kamb, and R. M. Frolich, Satellite radar interferometry for monitoring ice sheet motion: Application to an Antarctic ice stream, *Science*, 262, 1525–1530, 1993.
- Jet Propulsion Laboratory, Seasat (Interim Geophysical Data Record) user's handbook, initial version, altimeter, *NASA Rep.* 622-97, 1979.
- Kwok, R., and M. Fahnestock, Ice sheet motion and topography from radar interferometry, *IEEE Trans. Geosci. Remote Sens.*, 34(1), 189–200, 1996.
- Li, F., and R. M. Goldstein, Studies of multi-baseline spaceborne interferometric synthetic aperture radars, *IEEE Trans. Geosci. Remote Sens.*, 28(1), 88–97, 1990.
- Massonnet, D., and K. L. Feigl, Discrimination of geophysical phenomena in satellite radar interferograms, *Geophys. Res. Lett.*, 22(12), 1537–1540, 1995.
- Massonnet, D., M. Rossi, C. Carmona, F. Adragna, G. Peltzer, K. Feigl, and T. Rabaute, The displacement field of the Landers earthquake mapped by radar interferometry, *Nature*, 364, 138–142, 1993.
- Massonnet, D., K. Feigl, M. Rossi, and F. Adragna, Radar interferometric mapping of deformation in the year after the Landers earthquake, *Nature*, 369, 227–230, 1994.
- Massonnet, D., P. Briole, and A. Arnaud, Deflation of Mount Etna monitored by spaceborne radar interferometry, *Nature*, 375, 567–570, 1995.
- Moreira, J., M. Schwabisch, G. Fornaro, R. Lanari, R. Bamler, D. Just, U. Steinbrecher, H. Breit, M. Eineder, and G. Franceschetti, X-SAR interferometry: First results, *IEEE Trans. Geosci. Remote Sens.*, 33(4), 950–956, 1995.
- Peltzer, G., and P. Rosen, Surface displacement of the 17 May 1993 Eureka Valley, California earthquake observed by SAR interferometry, *Science*, 268, 1333–1336, 1995.
- Peltzer, G., K. W. Hudnut, and K. L. Feigl, Analysis of coseismic surface displacement gradients using radar interferometry: new insights into the Landers earthquake, *J. Geophys. Res.*, 99(B11), 21971–21981, 1994.
- Rignot, E., K. C. Jezek, and H. G. Sohn, Ice flow dynamics of the Greenland Ice Sheet from SAR interferometry, *Geophys. Res. Lett.*, 22(5), 575–578, 1995.
- Rocken, C., R. Ware, T. Van Hove, F. Solheim, C. Alber, J. Johnson, M. Bevis, and S. Businger, Sensing atmospheric water vapor with the Global Positioning System, *Geophys. Res. Lett.*, 20(23), 2631–2634, 1993.
- Rodriguez, E., and J. M. Martin, Theory and design of interferometric synthetic aperture radars, *IEE Proc., Part F*, 139(2), 147–159, 1992.
- Rosen, P. A., S. Hensley, H. A. Zebker, F. H. Webb, and E. Fielding, Surface deformation and coherence measurements of Kilauea Volcano, Hawaii from SIR-C radar interferometry, *J. Geophys. Res.*, 101(E10), 23,109–23,125, 1996.
- Saastamoinen, J., Atmospheric correction for troposphere and stratosphere in radio ranging of satellites, in *The Use of Artificial Satellites for Geodesy*, *Geophys. Monogr. Ser.*, vol. 15, edited by S. W. Henrikson, A. Mancini, and B. H. Chovitz, pp. 247–252, AGU, Washington, D. C., 1972.
- Smith, E. K., and S. Weintraub, The constants in the equation for atmospheric refractive index at radio frequencies, *Proc. IRE*, 41, 1035–1037, 1953.
- Stull, R. B., *An Introduction to Boundary Layer Meteorology*, Kluwer Acad., Norwell, Mass., 1988.
- Zebker, H., and R. M. Goldstein, Topographic mapping from interferometric synthetic aperture radar observations, *J. Geophys. Res.*, 91(B5), 4993–4999, 1986.
- Zebker, H. A., and J. Villasenor, Decorrelation in interferometric radar echoes, *IEEE Trans. Geosci. Remote Sens.*, 30(5), 950–959, 1992.
- Zebker, H. A., C. L. Werner, P. Rosen, and S. Hensley, Accuracy of topographic maps derived from ERS-1 radar interferometry, *IEEE Trans. Geosci. Remote Sens.*, 32(4), 823–836, 1994a.
- Zebker, H. A., P. A. Rosen, R. M. Goldstein, A. Gabriel, and C. Werner, On the derivation of coseismic displacement fields using differential radar interferometry: The Landers earthquake, *J. Geophys. Res.*, 99(B10), 19,617–19,634, 1994b.
- Zebker, H. A., T. G. Farr, R. P. Salazar, and T. H. Dixon, Mapping the world's topography using radar interferometry: The TOPSAT mission, *IEEE Proc.*, 82(12), 1774–1786, 1994c.
- Zebker, H. A., P. Rosen, S. Hensley, and P. J. Mouginiis-Mark, Analysis of active lava flows on Kilauea volcano, Hawaii, using SIR-C radar correlation measurements, *Geology*, 24(6), 495–498, 1996.

P. A. Rosen and S. Hensley, Jet Propulsion Laboratory, California Institute of Technology, 4800 Oak Grove Dr., MS 300-235, Pasadena, CA 91109. (e-mail: par@parsar.jpl.nasa.gov; sh@kaitak.jpl.nasa.gov)  
H. A. Zebker, 232 Durand, Department of Electrical Engineering, Stanford University, Stanford, CA 94305-9515. (e-mail: zebker@jakey.stanford.edu)

(Received June 20, 1996; revised November 27, 1996; accepted December 4, 1996.)